

# Ultrastrong steel via minimal lattice misfit and high-density nanoprecipitation

Suihe Jiang<sup>1</sup>, Hui Wang<sup>1</sup>, Yuan Wu<sup>1</sup>, Xiongjun Liu<sup>1</sup>, Honghong Chen<sup>1</sup>, Mengji Yao<sup>2</sup>, Baptiste Gault<sup>2</sup>, Dirk Ponge<sup>2</sup>, Dierk Raabe<sup>2</sup>, Akihiko Hirata<sup>3,4</sup>, Mingwei Chen<sup>3,5</sup>, Yandong Wang<sup>1</sup> & Zhaoping Lu<sup>1</sup>

Next-generation high-performance structural materials are required for lightweight design strategies and advanced energy applications. Maraging steels, combining a martensite matrix with nanoprecipitates, are a class of high-strength materials with the potential for matching these demands<sup>1–3</sup>. Their outstanding strength originates from semi-coherent precipitates<sup>4,5</sup>, which unavoidably exhibit a heterogeneous distribution that creates large coherency strains, which in turn may promote crack initiation under load<sup>6–8</sup>. Here we report a counterintuitive strategy for the design of ultrastrong steel alloys by high-density nanoprecipitation with minimal lattice misfit. We found that these highly dispersed, fully coherent precipitates (that is, the crystal lattice of the precipitates is almost the same as that of the surrounding matrix), showing very low lattice misfit with the matrix and high anti-phase boundary energy, strengthen alloys without sacrificing ductility. Such low lattice misfit ( $0.03 \pm 0.04$  per cent) decreases the nucleation barrier for precipitation, thus enabling and stabilizing nanoprecipitates with an extremely high number density (more than  $10^{24}$  per cubic metre) and small size (about  $2.7 \pm 0.2$  nanometres). The minimized elastic misfit strain around the particles does not contribute much to the dislocation interaction, which is typically needed for strength increase. Instead, our strengthening mechanism exploits the chemical ordering effect that creates backstresses (the forces opposing deformation) when precipitates are cut by dislocations. We create a class of steels, strengthened by Ni(Al,Fe) precipitates, with a strength of up to 2.2 gigapascals and good ductility (about 8.2 per cent). The chemical composition of the precipitates enables a substantial reduction in cost compared to conventional maraging steels owing to the replacement of the essential but high-cost alloying elements cobalt and titanium with inexpensive and lightweight aluminium. Strengthening of this class of steel alloy is based on minimal lattice misfit to achieve maximal precipitate dispersion and high cutting stress (the stress required for dislocations to cut through coherent precipitates and thus produce plastic deformation), and we envisage that this lattice misfit design concept may be applied to many other metallic alloys.

Figure 1a shows engineering stress–strain curves of the solution-annealed (15 min at 950 °C) and aged (3 h at 500 °C), Ni(Al,Fe)-maraging steels with a composition of Fe-18Ni3Al4Mo0.8Nb0.08C0.01B (wt%). The maximum yield strength is  $1,947 \pm 23$  MPa, together with an ultimate tensile strength of  $2,197 \pm 33$  MPa and a total elongation of  $8.2\% \pm 0.7\%$ . The newly developed steel shows a very high age-hardening response with an increase in yield strength by about 1,100 MPa, and practically no reduction in ductility upon ageing. This behaviour is in contrast to the loss in ductility of conventional maraging steels upon ageing<sup>5</sup> (see Fig. 1b), and exceeds the limits of the inverse strength–ductility relationship characteristic of high-strength

materials<sup>9–11</sup>. Particularly notable is the uniform-elongation regime, which increases from 1.9% to 3.8% upon ageing, far exceeding the values observed for other kinds of steel<sup>7,8</sup> at the same strength level. This observation indicates that the work-hardening capacity of the current steel is greatly enhanced when using highly coherent Ni(Al,Fe)-precipitates for ageing. In addition, the removal of the alloying elements Co and Ti reduces material costs (see details in Methods and Extended Data Fig. 1). Figure 1c and d shows typical bright-field scanning transmission electron microscopy (STEM) images of the solution-annealed and the aged Ni(Al,Fe)-maraging steel, respectively. The solution-annealed and quenched material assumes a typical lath martensite microstructure with high dislocation density. The selected area electron

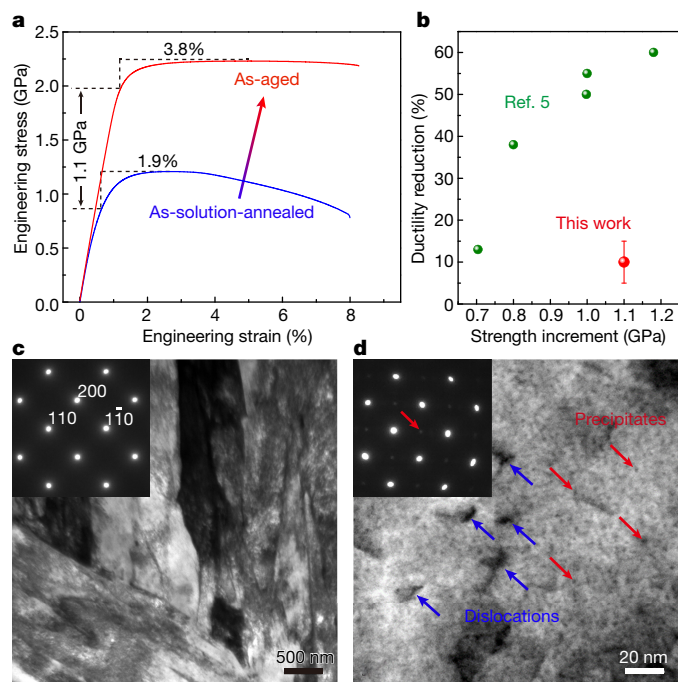


**Figure 1 | Mechanical properties and typical STEM images of the solution-annealed (15 min at 950 °C) and of the aged (3 h at 500 °C) Ni(Al,Fe)-maraging steels. a**, Tensile curves, the increment in yield stress and the change of uniform elongation (given in per cent) are highlighted. **b**, Change in ultimate tensile strength and ductility upon ageing observed for conventional maraging steels such as those presented in ref. 5 and in this work. **c**, **d**, Bright-field STEM images of the solution annealed and aged steel, respectively. The insets show the SAED patterns of the corresponding microstructure. The error bar on the red data point in **b** represents standard deviations from the mean for sets of five tests.

<sup>1</sup>State Key Laboratory for Advanced Metals and Materials, University of Science and Technology Beijing, Beijing 100083, China. <sup>2</sup>Department of Microstructure Physics and Alloy Design, Max-Planck-Institut für Eisenforschung GmbH, Max-Planck-Straße, Düsseldorf 40237, Germany. <sup>3</sup>WPI Advanced Institute for Materials Research, Tohoku University, Sendai 980-8577, Japan. <sup>4</sup>Mathematics for Advanced Materials-OIL, AIST-Tohoku University, Sendai 980-8577, Japan. <sup>5</sup>Department of Materials Science and Engineering, Johns Hopkins University, Baltimore Maryland 21218, USA.

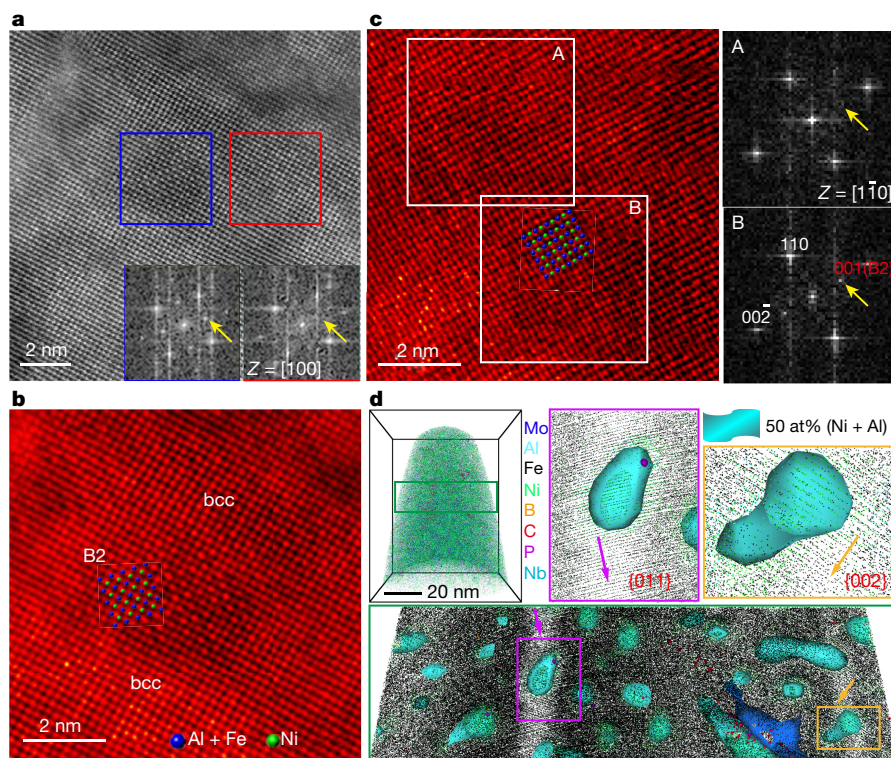


**Figure 2 | High-resolution HAADF STEM images and three-dimensional reconstruction of an APT dataset confirming the B2 nature of the precipitates with full lattice coherence.** **a**, STEM image taken from  $\langle 001 \rangle$  direction revealing B2 ordering, along with the inset showing the FFT (fast Fourier transform) patterns. **b**, Close-up image of **a** showing the periodic atomic columns. **c**, Atomic image taken from

$\langle 110 \rangle$ , with the corresponding FFT pattern shown in inset A also suggesting B2 ordering rather than  $D0_3$  ordering. Inset B in **c** is the FFT pattern of the matrix. **d**, Thin slice (bottom panel of **d**) through the APT dataset (top left panel of **d**) showing two families of atomic planes—the  $\{011\}$  and  $\{002\}$  planes—with perfect continuity imaged in the tomographic reconstruction.

diffraction (SAED) pattern (inset in Fig. 1c) from the  $\langle 100 \rangle_{\alpha}$  zone axis exhibits a typical body-centred cubic (bcc) structure without extra super-lattice diffraction spots. After ageing, the microstructure has dramatically changed. Fig. 1d reveals precipitation of a very high number density of ultrafine (2–5 nm) spherical precipitates with a highly uniform distribution. The inset in Fig. 1d shows the corresponding SAED pattern, in which the weak spots are identified as  $\{100\}$  from an ordered B2 structured phase, and no other precipitates were detected. The dark line contrast in the image indicates that a high density of dislocations prevails even after the ageing process.

The atomic structures of the aged samples were further characterized by high-angle annular dark-field (HAADF) STEM and atom probe tomography (APT) (Fig. 2). The fast Fourier transform patterns of the image (Fig. 2a) taken from the  $\langle 100 \rangle$  zone axis show that the matrix is still bcc-structured and the precipitates have an ordered B2 structure. However, no sharp particle/matrix interfaces were observed, that is, the precipitates seem to be highly coherent with the matrix. The zoom-in image of a precipitate (Fig. 2b) along the  $\langle 100 \rangle$  direction shows the atomic columns with periodically strong and weak intensity, corresponding to the B2 ordering. The contrast in HAADF imaging originates from low atomic numbers ( $Z$ ), hence, dark columns are supposed to arise from the partitioning of Al atoms. Also, some irregular intensity variations in the dark columns indicate that some of the Al-atomic sites in the B2 structure are partially replaced by heavier atoms. To further characterize the atomic structure of the precipitates, Fig. 2c shows an image taken along the  $\langle 110 \rangle$  direction, confirming that the particles are indeed of B2 Ni/Al-rich structure. A thin slice through a reconstruction of an APT dataset, calibrated based on methods described previously<sup>12,13</sup>, is shown in Fig. 2d, which reveals the presence of two sets of atomic planes, namely  $\{011\}$  and  $\{002\}$ . In the region where the  $\{011\}$  and  $\{002\}$  planes are imaged, we observed that they continue perfectly through the precipitates, suggesting full

lattice coherency with the matrix. This result is consistent with the transmission electron microscope (TEM) observations and the results reported for other types of alloys<sup>14</sup>.

Details of the microstructure and elemental composition of the precipitates were characterized by APT. Figure 3a shows the tomographic reconstruction from one of the APT datasets, revealing a large volume fraction of precipitates with a number density of about  $3.7 \times 10^{24} \text{ m}^{-3}$ , as highlighted by an isoconcentration surface. To our surprise, the number density of nanoprecipitates in the current alloy is several times higher than that reported for conventional precipitation-hardened metallic materials such as traditional maraging steels<sup>5</sup> or for Ni/Al-strengthened alloys with high strength<sup>15–18</sup>. This observation shows that lattice misfit design enables the formation of nanoprecipitates with an extremely high number density. Although most precipitates assume a near-spherical shape, some are elongated. Several linear features can be revealed by the isoconcentration envelopes surrounding zones in the data containing a high concentration of Mo and interstitial impurities (C, B and P), as shown in Fig. 3b. We suggest that these features are due to segregation along dislocations<sup>19,20</sup>, which was also revealed by correlating APT with TEM<sup>21</sup>. The larger precipitates imaged are mostly found in the vicinity of, or in contact with these dislocations, and tend to be more elongated (Fig. 3c). By making use of proximity histograms<sup>22</sup>, calculated from the isoconcentration surfaces shown in Fig. 3d, the compositions of precipitates with various shapes were obtained (Extended Data Fig. 2). The corresponding mass spectrum from the precipitates is also presented in Extended Data Fig. 3, which shows why the concentration of Al and Fe can be accurately determined (see details in Methods). These analyses reveal that all precipitates, irrespective of their sizes, shapes or nucleation sites, are chemically similar, and their composition averaged over all morphologies is  $45.7 \pm 1.6$  at% Ni,  $28.4 \pm 2.0$  at% Al and  $25.6 \pm 2.1$  at% Fe. The ratio of Ni:(Al,Fe) is approximately 1,

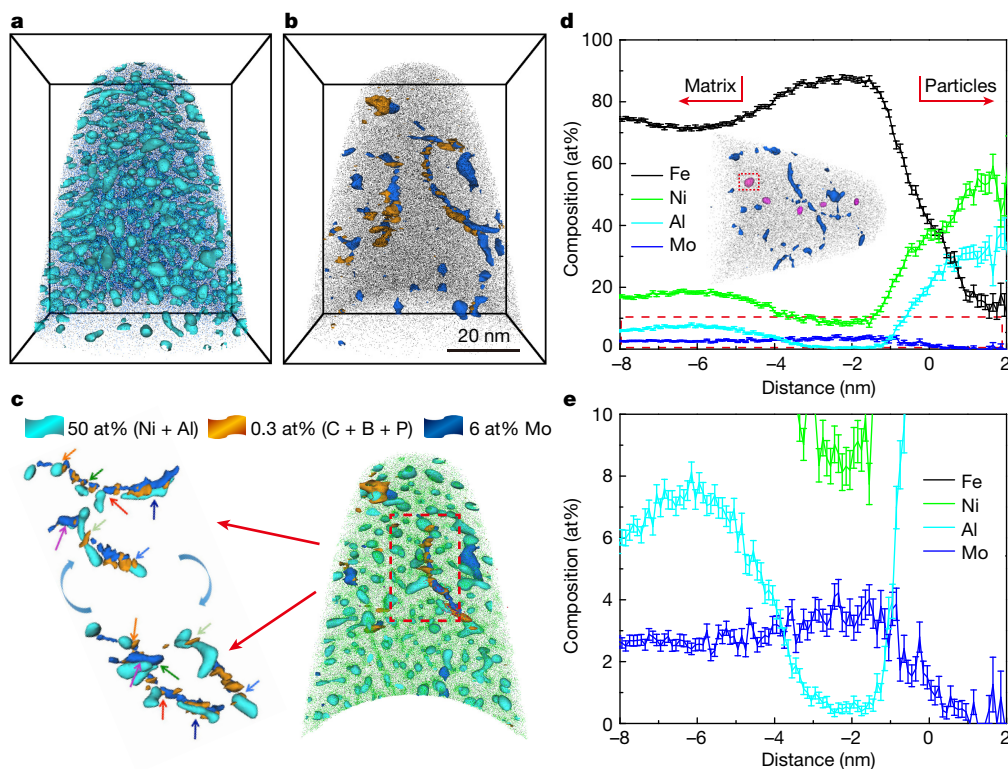


**Figure 3 | Atom probe analysis showing tomography and composition of the precipitates.** **a**, Precipitates highlighted by an isoconcentration surface encompassing regions containing more than 50 at% of Al and Ni combined. **b**, Isoconcentration surfaces encompassing zones containing more than 6 at% of Mo and 0.3 at% of interstitial impurities (C, P and B), highlighting the presence of elongated decoration zones revealing segregation to dislocations. **c**, Precipitates growing near or at dislocations

which confirms that Al-atomic sites in B2 as observed by the HAADF STEM (Fig. 2b) are substituted by Fe, suggesting a B2 Ni(Al,Fe) phase. The proximity histogram in Fig. 3d and the corresponding close-up image (Fig. 3e) reveal that Mo is repelled from the precipitates. It reaches a concentration of about 2.5 at% in the matrix and heavily segregates to dislocations. In addition, the precipitates are surrounded by a region depleted in solutes such as Ni and Al that extends over several nanometres. Further away from the precipitate/matrix interfaces, the matrix composition assumes the nominal solution state. These features indicate that particle growth is dominated by short-range reshuffling of the constituents, and long-range diffusion is suppressed.

We further conducted synchrotron experiments to investigate the phase formation and examine the lattice mismatch between precipitates and matrix. Figure 4a shows synchrotron X-ray diffraction (XRD) patterns of the solution-annealed and aged samples. The black arrow marks the  $\{100\}_{B2}$  superlattice reflections, which are observed only in the diffraction pattern of the aged samples, and the broadening of this peak also indicates the ultrasmall size of the B2 precipitates. It is worth noting that the particles have a mono-domain structure with no or limited defect contents, as shown in the high-resolution STEM images in Fig. 2. The width of the XRD peaks depends on the average size of the particles and on the micro-strain fields surrounding them. Thus, to quantitatively analyse the line broadening, the modified Williamson–Hall<sup>23,24</sup> plots of the widths of the XRD diffraction peaks versus  $KC^{1/2}$  ( $K = 2\sin(\theta)/\lambda$ ) were used as shown in Fig. 4b, where  $\theta$  is the Bragg angle,  $\lambda$  is the wavelength of the X-rays and  $C$  is the average contrast factor of dislocations in the case of a particular reflection. The width of the  $\{100\}_{B2}$  peak is much larger than that generated by strain broadening in the low- $K$  regime. By subtracting the strain contribution, the average diameter was then determined to be  $2.7 \pm 0.2$  nm, consistent with the

as indicated by the straight coloured arrows pointing to the same precipitate imaged in two projections. **d**, Proximity histogram showing the composition change across the selected precipitates; the inset indicates the particle (surrounded by a dotted rectangle) that was analysed. **e**, Corresponding close-up image (of the region in **d** indicated by the dashed rectangle) with different ordinate height revealing the rejection of Mo atoms out of the precipitates. The error bars are standard deviations of the mean.

TEM and APT data. Despite the slight recovery occurring during ageing as indicated by the weak decrease in slope of the fitted straight line, the martensitic matrix maintains a very high dislocation density. These dislocations have important roles both in precipitation behaviour and in the mechanical properties of the alloy. A series of extremely weak XRD peaks within the angular range  $1^\circ$ – $4^\circ$  (inset in Fig. 4a) also appears for all specimens. These could be indexed as NbC (Extended Data Fig. 4). The intensity of the diffraction peaks after ageing is basically unchanged, except for that of the B2 peaks. All these observations suggest that B2-structured Ni(Al,Fe) precipitates are the prevalent nanophase formed during ageing.

The lattice parameters of the B2 and of the martensite phases in both conditions were calculated from the XRD peaks (Extended Data Fig. 5). The results from the fitting procedure suggest that the lattice parameters of the solution-annealed bcc matrix, the aged bcc matrix and the B2 precipitates are  $2.881 \pm 0.0003$  Å,  $2.877 \pm 0.0002$  Å and  $2.882 \pm 0.0012$  Å, respectively. For the current coherent alloy, the lattice mismatch for B2 precipitates changes from  $0.03\% \pm 0.04\%$  during the early nucleation stage to  $0.17\% \pm 0.04\%$  during the later stages of precipitation owing to the gradual elemental partitioning among the two phases (see Methods for the calculation details). This change in lattice misfit enables an ideal, minimal nucleation barrier at the onset of precipitation and increasing dislocation interaction during the later stages. It should be noted that the lattice constant of stoichiometric NiAl is 0.2887 nm, close to that of ferritic steels<sup>18</sup>, that is, 0.2866 nm. Yet APT revealed that large atoms such as Mo, Nb and Al are present in the matrix, expanding its bcc lattice to 0.2881 nm (Extended Data Fig. 5). APT also shows that the Ni(Al,Fe) nuclei contain up to 25.6 at% Fe, which occupies the Al-atomic sites and further decreases its lattice parameter<sup>25</sup>. In combination, we can realize an ultralow lattice mismatch of  $0.03\% \pm 0.04\%$  in this system, which effectively lowers

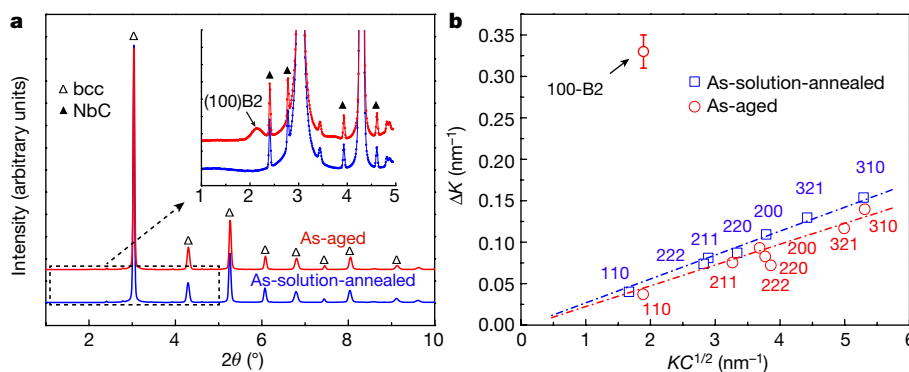


**Figure 4 | Synchrotron XRD results showing the overall phase transformation and extremely low lattice misfit between bcc matrix and B2 precipitates.** **a**, Synchrotron XRD patterns of the solution-annealed and aged specimens. The inset shows the presence of broadened peaks pertaining to B2 after ageing. The lattice parameter of the matrix and of

the elastic misfit energy between the nuclei of the particles and the matrix. In conjunction with the low interfacial energy<sup>26</sup> of Ni(Al,Fe) in the bcc matrix of about  $35 \text{ mJ m}^{-2}$ , the energy barrier for homogeneous nucleation is drastically decreased, promoting homogeneous nucleation of the B2 Ni(Al,Fe) phase. Although elongated precipitates at dislocations were observed by APT (Fig. 3), their volume fraction is below 5%, and homogeneous nucleation is hence the prevalent formation mechanism leading to the observed high number density of Ni(Al,Fe) nanoprecipitates (about  $3.7 \times 10^{24} \text{ m}^{-3}$ ).

For a system with a large volume fraction of nanoprecipitates and a high dislocation density, precipitate stabilization must be considered. As shown in Fig. 3d, precipitate growth and coarsening are both controlled by long-range diffusion. This effect results in slow growth of the precipitates. Precipitates formed at dislocations, though, assume slightly elongated shapes owing to the more rapid pipe diffusion mechanism. Mo atoms get rejected from the precipitates upon growth. When considering that the diffusivity of Mo is much lower than that of the other constituents in  $\alpha$ -Fe at  $500^\circ\text{C}$  (see details in Methods and Extended Data Table 1), we suggest that this kinetic bottleneck effectively suppresses rapid coarsening of precipitates, thus promoting maintenance of the highly uniform microstructure and the small particle size. The drastically reduced lattice misfit between the matrix and precipitates also stabilizes the coherent interface by lowering the elastic strain energy<sup>27</sup>, favouring near-spherical particle morphology and reducing the driving force for competitive coarsening. This means that Mo acts twofold, namely, through its slow kinetics when being rejected upon precipitate growth and through its effect on the reduction of the lattice mismatch between matrix and nanoprecipitates. As a result, the addition of Mo effectively reduces the size, enhances the stability and increases the number density of the B2 nanoprecipitates.

Owing to their extremely fine size ( $2.7 \pm 0.2 \text{ nm}$ ) and very high number density (about  $3.7 \times 10^{24} \text{ m}^{-3}$ ), the coherent precipitates strengthen the matrix via dislocation shearing: lattice dislocations cut the precipitates in order to progress through the material. In the current system, with a low coherency strain, strengthening from elastic coherency strains is negligible. Instead, ordering and modulus hardening prevail as strengthening mechanisms. The contribution of these two factors to the total yield strength is estimated to be 245 MPa and 812 MPa, respectively (see details in Methods). Assuming additivity of these two strengthening mechanisms, the total increment amounts to 1,057 MPa, which agrees with the experimental result of 1,100 MPa. This estimate suggests that the ordering has the dominant role in controlling the strengthening while modulus hardening is less important.

Although a relatively high content of carbon was added to the Ni(Al,Fe)-maraging steel, the resulting tensile ductility remains almost the same even after ageing. This combination of high strength and good ductility is attributed to the following two aspects. First, the high

the B2 phase was calculated from the XRD data. **b**, Modified Williamson-Hall plot for the solution-annealed and aged steels. The dash-dotted lines are the linear fits obtained by the method of least squares, indicating the lattice distortion through dislocations. The errors in  $\Delta K$  are associated with the errors in the experimental measurements of  $\Delta\theta$ .

homogeneity of the distribution of the Ni(Al,Fe) precipitates effectively reduces stress concentrations, which is a main challenge in traditional maraging steels<sup>6–8</sup>. In addition, the precipitates are very small and their lattice parameter is similar to that of the martensitic matrix. The associated elastic interaction between precipitates and cutting dislocations is hence lowered, thereby preventing crack initiation at the precipitate-matrix interfaces owing to negligible strain accumulation. Second, the high content of solute Ni in the matrix has an important role in reducing the tendency for cleavage, lowering the ductile-brittle transition temperature of steels<sup>2</sup>. As a primary precipitate-forming element in maraging steels, its residual content in the matrix is in the current alloy controlled by the precipitates that absorb Ni. Compared to the dominant strengthening phases in traditional 18Ni maraging steels—such as  $\text{Ni}_3\text{Ti}$  and  $\text{Ni}_3\text{Mo}$ —which require stoichiometric composition<sup>28</sup>, the current Ni(Al,Fe) precipitates are not only finer and denser, but also consume less Ni. Therefore, the class of Ni(Al,Fe)-maraging steels described here shows an advantage in saving solute Ni for the matrix, which also contributes to its unusual combination of high strength and good ductility.

**Online Content** Methods, along with any additional Extended Data display items and Source Data, are available in the online version of the paper; references unique to these sections appear only in the online paper.

Received 30 August 2016; accepted 2 February 2017.

Published online 10 April; corrected online 26 April 2017

(see full-text HTML version for details).

- Decker, R. F. & Floreen, S. in *Maraging Steels: Recent Developments and Applications* (ed. Wilson, R. K.) 1–38 (TMS-AIME, 1988).
- Floreen, S. The physical metallurgy of maraging steels. *Metall. Rev.* **13**, 115–128 (1968).
- Raabe, D., Ponge, D., Dmitrieva, O. & Sander, B. Nanoprecipitate-hardened 1.5GPa steels with unexpected high ductility. *Scr. Mater.* **60**, 1141–1144 (2009).
- Tewari, R. *et al.* Precipitation in 18 wt% Ni maraging steel of grade 350. *Acta Mater.* **48**, 1187–1200 (2000).
- Sha, W. & Guo, Z. *Maraging Steels: Modelling of Microstructure, Properties and Applications* 1st edn, 63 (Woodhead, 2009).
- Ashby, M. F. Work hardening of dispersion-hardened crystals. *Phil. Mag.* **14**, 1157–1178 (1966).
- Ooi, S. W., Hill, P., Rawson, M. & Bhadeshia, H. D. Effect of retained austenite and high temperature Laves phase on the work hardening of an experimental maraging steel. *Mater. Sci. Eng. A* **564**, 485–492 (2013).
- Viswanathan, U. K., Dey, G. K. & Asundi, M. K. Precipitation hardening in 350 grade maraging steel. *Metall. Trans. A* **24**, 2429–2442 (1993).
- Ritchie, R. O. The conflicts between strength and toughness. *Nat. Mater.* **10**, 817–822 (2011).
- Lu, K., Lu, L. & Suresh, S. Strengthening materials by engineering coherent internal boundaries at the nanoscale. *Science* **324**, 349–352 (2009).
- Li, Z. M. *et al.* Metastable high-entropy dual-phase alloys overcome the strength-ductility trade-off. *Nature* **534**, 227–230 (2016).
- Gault, B. *et al.* Advances in the calibration of atom probe tomographic reconstruction. *J. Appl. Phys.* **105**, 034913 (2009).
- Moody, M. P. *et al.* Qualification of the tomographic reconstruction in atom probe by advanced spatial distribution map techniques. *Ultramicroscopy* **109**, 815–824 (2009).

14. Gault, B. *et al.* Atom probe tomography investigation of Mg site occupancy within  $\delta'$  precipitates in an Al–Mg–Li alloy. *Scr. Mater.* **66**, 903–906 (2012).
15. Kapoor, M. *et al.* Aging characteristics and mechanical properties of 1600 MPa body-centered cubic Cu and B2-NiAl precipitation-strengthened ferritic steel. *Acta Mater.* **73**, 56–74 (2014).
16. Jiao, Z. B. *et al.* Precipitation mechanism and mechanical properties of an ultra-high strength steel hardened by nanoscale NiAl and Cu particles. *Acta Mater.* **97**, 58–67 (2015).
17. Guo, Z., Sha, W. & Vaumousse, D. Microstructural evolution in a PH13–8 stainless steel after ageing. *Acta Mater.* **51**, 101–116 (2003).
18. Ping, D. H. *et al.* Microstructural evolution in 13Cr–8Ni–2.5Mo–2Al martensitic precipitation-hardened stainless steel. *Mater. Sci. Eng. A* **394**, 285–295 (2005).
19. Blavette, D., Cadel, E., Fraczkiewicz, A. & Menand, A. Three-dimensional atomic-scale imaging of impurity segregation to line defects. *Science* **286**, 2317–2319 (1999).
20. Smith, G. D. W., Hudson, D., Styman, P. D. & Williams, C. A. Studies of dislocations by field ion microscopy and atom probe tomography. *Phil. Mag.* **93**, 3726–3740 (2013).
21. Kuzmina, M. *et al.* Linear complexions: confined chemical and structural states at dislocations. *Science* **349**, 1080–1083 (2015).
22. Hellman, O. C. *et al.* Analysis of three-dimensional atom-probe data by the proximity histogram. *Microsc. Microanal.* **6**, 437–444 (2000).
23. Williamson, G. K. & Hall, W. H. X-ray line broadening from fcc aluminium and wolfram. *Acta Metall.* **1**, 22–31 (1953).
24. Ungár, T. & Borbély, A. The effect of dislocation contrast on x-ray line broadening: a new approach to line profile analysis. *Appl. Phys. Lett.* **69**, 3173–3175 (1996).
25. Teng, Z. K. *et al.* Neutron-diffraction study and modeling of the lattice parameters of a NiAl-precipitate-strengthened Fe-based alloy. *Acta Mater.* **60**, 5362–5369 (2012).
26. Sonderegger, B. & Kozeschnik, E. Generalized nearest-neighbor broken-bond analysis of randomly oriented coherent interfaces in multicomponent fcc and bcc structures. *Metall. Mater. Trans. A* **40**, 499–510 (2009).
27. Lu, K. Stabilizing nanostructures in metals using grain and twin boundary architectures. *Nat. Rev. Mater.* **1**, 16019 (2016).
28. Sha, W., Cerezo, A. & Smith, G. D. W. Phase chemistry and precipitation reactions in maraging steels. Part III. Model alloys. *Metall. Trans. A* **24**, 1241–1249 (1993).

**Acknowledgements** This research was supported by the National Natural Science Foundation of China (grant numbers 51531001, 51422101, 51671018, 51271212 and 51371003), the 111 Project (grant number B07003), the International S&T Cooperation Program of China (grant number 2015DFG52600), the Program for Changjiang Scholars and Innovative Research Team in University (grant number IRT\_14R05) and the Projects of SKL-AMM-USTB (grant numbers 2016Z-04, 2016-09, 2016Z-16). Y.W. acknowledges the Top-Notch Young Talents Program and the Fundamental Research Funds for the Central Universities. We thank X. Xu at Tongling University, Z. Fan at the China Academy of Engineering Physics, Y. Qiao, L. You and G. Liu at the University of Science and Technology Beijing, and Y. Tian at Tohoku University for help with sample preparation and discussions. M.Y. and B.G. are grateful to U. Tezins and A. Sturm for their support of the focused ion beam and APT facilities at the Max-Planck-Institut für Eisenforschung. This research used resources of the Advanced Photon Source, a US Department of Energy (DOE) Office of Science User Facility operated for the DOE Office of Science by Argonne National Laboratory under contract number DE-AC02-06CH11357.

**Author Contributions** Z.L. designed the study. S.J., H.C., H.W., X.L. and Y. Wu carried out the main experiments. S.J., H.W., Z.L. and D.R. analysed the data and wrote the main draft of the paper. M.Y., B.G., D.P. and D.R. prepared the APT samples and interpreted the results. M.C. and A.H. conducted the STEM characterization. Y.W. conducted the synchrotron experiments. All authors contributed to the discussion of the results, and commented on the manuscript.

**Author Information** Reprints and permissions information is available at [www.nature.com/reprints](http://www.nature.com/reprints). The authors declare no competing financial interests. Readers are welcome to comment on the online version of the paper. Publisher's note: Springer Nature remains neutral with regard to jurisdictional claims in published maps and institutional affiliations. Correspondence and requests for materials should be addressed to Z.P.L. ([luzp@ustb.edu.cn](mailto:luzp@ustb.edu.cn)).

**Reviewer Information** *Nature* thanks M. Moody, J. Morris Jr and the other anonymous reviewer(s) for their contribution to the peer review of this work.

## METHODS

**Specimen preparation.** Alloy ingots with a nominal composition of Fe-18Ni3Al4Mo0.8Nb0.08C0.01B (wt%) were prepared by arc-melting using elemental ingredients with a purity above 99.9 at%. The ingots were re-melted at least eight times and then drop-cast into a 10 mm × 10 mm × 80 mm copper mould. The as-cast bars were first homogenized at 1,200 °C for 24 h under Ar atmosphere, then cold rolled to a total reduction of around 70%, and subsequently annealed at 950 °C for 15 min, followed by water quenching. The specimens were then aged at 500 °C for 3 h. Sheet tensile samples with a gauge length of 20 mm and cross-section of 3 mm × 1.2 mm were cut and mechanically polished to 2,000 grit size. Tensile tests were conducted on a Mechanical Testing & Simulation (MTS) machine at a strain rate of  $5 \times 10^{-3}$ .

**Comparison of raw material cost.** Extended Data Fig. 1 shows the correlation between the maximum tensile strength and the raw material costs for the steels studied, in comparison to typical ultrahigh-strength steels reported in the literature, including the commercially successful 18 wt% Ni maraging steels (Ni18Co9Mo5, wt%)<sup>1</sup>, Co-free maraging steels (Ni18.5Mo4Ti, wt%)<sup>2</sup>, W-strengthened steel (Ni19W4.2Ti1.2, wt%)<sup>29</sup>, and some commercial ultrahigh-strength steels (for example, Ni11Co13Cr3, wt%)<sup>30</sup>. As can be seen, such compositional alloy tolerance not only produces impressive mechanical properties, but also much lower raw material costs than currently available ultrahigh-strength steels. More importantly, a certain tolerable carbon concentration in the current steels will also greatly facilitate alloy preparation and reduce refinement efforts.

**Microstructure characterization.** STEM observations were conducted on a JEOL JEM-2100 F instrument equipped with double spherical aberration correctors for probe forming and image forming lenses. HAADF STEM images were taken using an annular-type detector with a collection angle ranging from 100 mrad to 267 mrad, while bright-field STEM images were simultaneously recorded using a STEM bright-field detector.

**APT.** APT experiments were performed on a Cameca LEAP 5000 XS. This instrument is equipped with a new generation of micro-channel plates used at the entry face of the detector which allows for approximately 80% of the ions to be detected. Specimens for APT were prepared in a scanning electron microscope/focused-ion beam, using the lift-out procedure outlined in ref. 31. The data was acquired at a base temperature of 60 K, using high-voltage pulses, the amplitude of which was 15% of the applied direct-current voltage, at a repetition rate of 200 kHz. The high voltage was progressively increased to maintain a detection rate of 5 ions per 1,000 pulses. The APT data was reconstructed using Cameca IVAS 3.6.12 using the protocol described in ref. 32 and the reconstruction was calibrated based on elements of crystallography retained within the data<sup>12</sup> characterized by spatial distribution maps<sup>13</sup>.

Regarding the potential overlap between Al<sup>+</sup> and Fe<sup>2+</sup> at 27 Da in the APT mass spectrum, the detection of <sup>27</sup>Al<sup>+</sup> should be revealed by an analysis of the isotopic ratio of Fe. For a subset of the data containing approximately 720,000 ions, we counted 28,817 ions in the <sup>54</sup>Fe<sup>2+</sup> peak and 452,815 in the <sup>56</sup>Fe<sup>2+</sup> peak, which reflects the natural isotopic abundance of Fe within 0.10%. Assuming that 99.9% of Al was present as <sup>27</sup>Al<sup>2+</sup>, 41 ions of <sup>27</sup>Al<sup>+</sup> should be detected as part of the <sup>54</sup>Fe<sup>2+</sup> peak. This is, however, unlikely as it worsens the Fe isotopic ratio. This subset of the data contains 40 precipitates, shown in Extended Data Fig. 3, and when these are isolated, the mass spectrum contains 1,865 ions in the <sup>54</sup>Fe<sup>2+</sup> peak and 29,387 ions in the <sup>56</sup>Fe<sup>2+</sup> peak, which is within 0.38% of the natural isotopic ratio of Fe. Stronger evidence for the absence of overlap between Al and Fe can be found in the analysis of the charge-state ratio for the different species. The mass-to-charge ratio spectrum reveals no Ni<sup>1+</sup> or Fe<sup>1+</sup> above the background level. According to the post-ionization theory<sup>33</sup>, based on the charge-state ratio of both Ni and Fe, the expected electric field is at least in the range of 29–31 V nm<sup>-1</sup>. In this range, at least 99.9% of Al should be detected as <sup>27</sup>Al<sup>2+</sup>. Additional evidence points to an even higher electric field: a peak appears at around 9 Da for <sup>27</sup>Al<sup>3+</sup>, and based on the proportion of this particular charge state, the field is expected to be 33–34 V nm<sup>-1</sup>. These details and additional analyses provide evidence that the peak at 27 Da can be exclusively attributed to <sup>54</sup>Fe<sup>2+</sup>.

**Synchrotron radiation and lattice parameter determination.** Synchrotron radiation was also applied to examine structure evolution during the ageing treatment, and experiments were performed on the 11-ID-C beam line of the Advanced Photon Source, Argonne National Laboratory, USA. A monochromatic X-ray beam with an energy of 115 keV (with wavelength 0.010801 nm) was used. We checked the lattice parameter of the solution-annealed and the aged samples by measuring the position of each peak in the synchrotron scattering X-ray data. The measured lattice parameters from each peak were then plotted versus  $f(\theta) = \cos^2(\theta) \times (1/\sin\theta + 1/\theta)/2$ , where  $\theta$  is the Bragg angle for each peak<sup>34</sup>. As shown in Extended Data Fig. 5, the best value of the lattice parameter can thus be extrapolated from the linear regression, that is, the value at  $f(\theta) = 0$ . Clearly, the lattice parameter of the annealed matrix with Mo and Al additions was increased to a value very close to that of the Ni(Al,Fe) precipitates. The lattice mismatch between matrix and B2 precipitates was then estimated by the equation  $\delta = 2(\alpha_{B2} - \alpha_{matrix})/(\alpha_{matrix} + \alpha_{B2})$ , where  $\alpha$  refers to the respective lattice parameter of each phase.

**Effects of Mo additions on stability of B2 precipitates.** According to the Lifshitz–Slyozov–Wagner (LSW) theory, interfacial energy and diffusivity of partitioning elements are the two key factors controlling capillary-driven coarsening. Owing to the small size and low lattice misfit, addition of 2.5 at% Mo to our new alloy did not much alter the total interfacial energy. For a rough estimation of the coarsening process, we compiled the diffusion coefficients<sup>35–38</sup> of the partitioning elements in the  $\alpha$ -Fe matrix (Extended Data Table 1). As shown, the diffusivity of Mo is much lower than that of the other constituents. This means that Mo acts as the kinetically controlling element of the coarsening process, as revealed by the fact that Mo is rejected from the precipitate into the matrix, accumulating before the interface. The averaged interparticle spacing is estimated to be about 11 nm from the APT data. Thus, the diffusion time for Mo is about 7 h. Without Mo, the kinetically controlling element would have been Fe (Extended Data Table 1), which would have reduced this diffusion time down to 2 h with the assumption that the interparticle spacing is unchanged. Therefore, Mo acts twofold; first, it retards coarsening of the B2 precipitates through its rejection into the matrix and its accumulation before the interface (Fig. 3d and e). Its very slow kinetics thus controls particle growth and competitive capillary-driven ripening of particles. Second, Mo reduces the lattice mismatch between matrix and nanoprecipitates, hence reducing the elastic misfit energy as a driving force for coarsening.

**Estimation of strengthening response.** For modulus hardening, the stress increment can be described by the Knowles–Kelly equation<sup>39</sup>

$$\Delta\sigma_{\text{modulus}} = \frac{M\Delta G}{4\pi^2} \left( \frac{3\Delta G}{Gb} \right)^{1/2} \left[ 0.8 - 0.143 \ln \left( \frac{r}{b} \right) \right]^{2/3} r^{1/2} f^{1/2} \quad (1)$$

where  $M \approx 3$  is the Taylor factor,  $b = 0.249$  nm is the Burgers vector of the dislocation,  $r$  is the mean radius of the Ni(Al,Fe) particles and  $G = 71$  GPa is the modulus of the matrix.  $\Delta G$  is the difference in the shear modulus between the matrix and precipitates. The modulus of the B2 phase was reported to be about 88 GPa which is not strongly composition-dependent<sup>40</sup> and  $f = (4/3)\pi n r^3$  is the volume fraction of the Ni(Al,Fe) nanoprecipitates, where  $n$  is the number density of the precipitates.

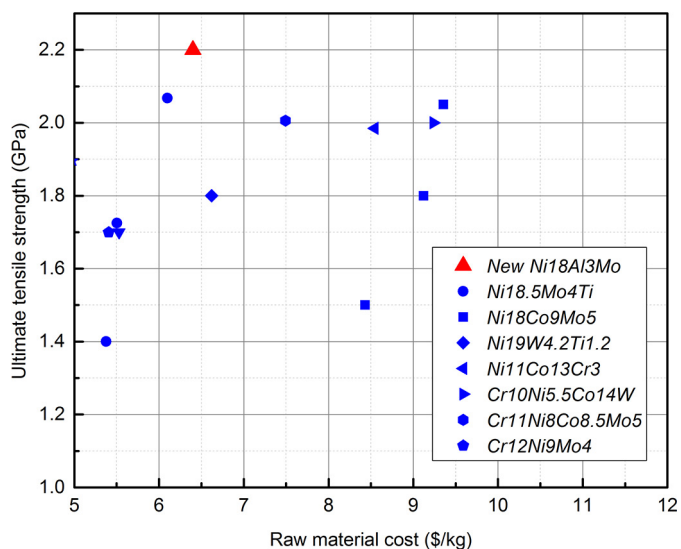
For ordering hardening, the stress increment can be estimated by<sup>41</sup>

$$\Delta\sigma_{\text{ordering}} = \frac{M\gamma_{\text{apb}}^{3/2}}{b} \left( \frac{4r_s f}{\pi T_1} \right)^{1/2} \quad (2)$$

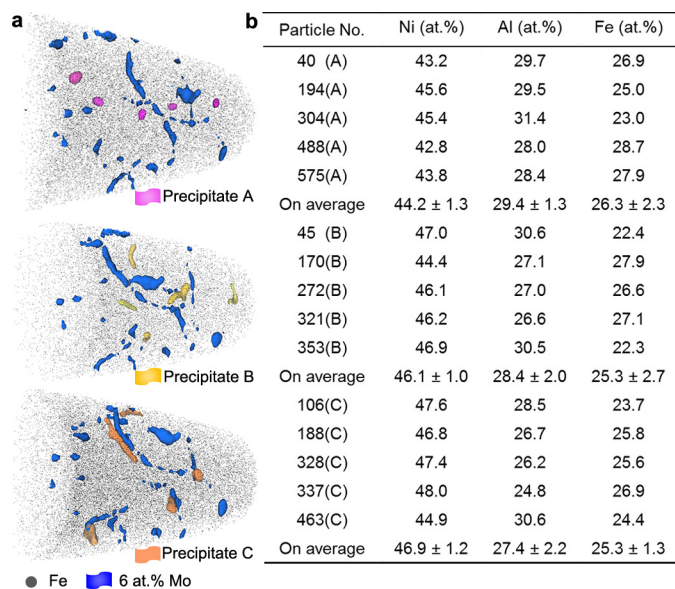
where  $r_s = (2/3)^{1/2} r$  is the average radius of the sheared precipitates in the gliding plane,  $\gamma_{\text{apb}} = 0.5$  J m<sup>-2</sup> is the average value<sup>42,43</sup> of the antiphase boundary energy for B2 Ni(Al,Fe) and  $T_1$  is the dislocation line tension, which can be approximated as  $Gb^2/2$ . The calculated results for the two contributions are 245 MPa and 812 MPa, respectively.

**Data availability.** The datasets generated during and/or analysed during the current study are available from the corresponding author on reasonable request.

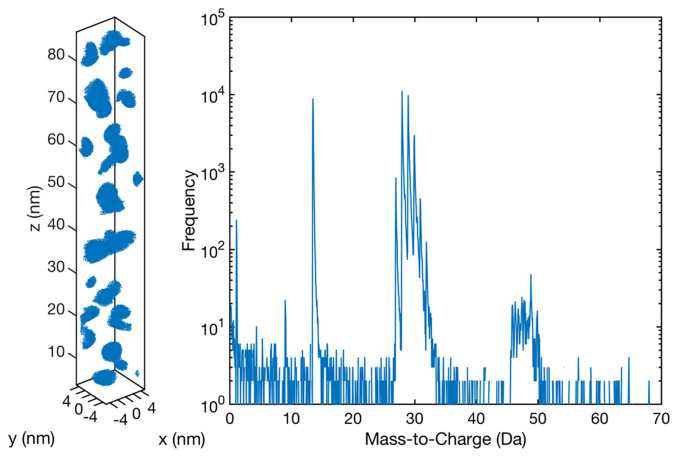
29. Kim, Y. G., Kim, G. S., Lee, C. S. & Lee, D. N. Microstructure and mechanical properties of a cobalt-free tungsten-bearing maraging steel. *Mater. Sci. Eng.* **79**, 133–140 (1986).
30. Pereloma, E. & Edmonds, D. V. *Phase Transformations in Steels: Diffusionless Transformations, High strength steels, Modelling and Advanced Analytical Techniques* 1st edn, 335 (Woodhead, 2012).
31. Thompson, K. *et al.* In situ site-specific specimen preparation for atom probe tomography. *Ultramicroscopy* **107**, 131–139 (2007).
32. Gault, B. *et al.* Advances in the reconstruction of atom probe tomography data. *Ultramicroscopy* **111**, 448–457 (2011).
33. Kingham, D. R. The post-ionization of field evaporated ions: a theoretical explanation of multiple charge states. *Surf. Sci.* **116**, 273–301 (1982).
34. Nelson, J. B. & Riley, D. P. An experimental investigation of extrapolation methods in the derivation of accurate unit-cell dimensions of crystals. *Proc. Phys. Soc.* **57**, 160–177 (1945).
35. Nitta, H. *et al.* Diffusion of molybdenum in  $\alpha$ -iron. *Acta Mater.* **50**, 4117–4125 (2002).
36. Hettich, G., Mehrer, H. & Maier, K. Self-diffusion in ferromagnetic  $\alpha$ -iron. *Scr. Metall.* **11**, 795–802 (1977).
37. Bergner, D. & Khaddour, Y. Impurity and chemical diffusion of Al in bcc and fcc iron. *Defect Diffus. Forum.* **95**, 709–714 (1993).
38. Gale, W. F. & Totemeier, T. C. *Smithells Metals Reference Book* 8th edn, 13–60 (Butterworth-Heinemann, 2003).
39. Kelly, P. Progress report on recent advances in physical metallurgy: (C) The quantitative relationship between microstructure and properties in two-phase alloys. *Int. Metall. Rev.* **18**, 31–36 (1973).
40. Baker, I. A review of the mechanical properties of B2 compounds. *Mater. Sci. Eng. A* **192–193**, 1–13 (1995).
41. Gladman, T. Precipitation hardening in metals. *Mater. Sci. Technol.* **15**, 30–36 (1999).
42. Noebe, R. D., Bowman, R. R. & Nathal, M. V. Physical and mechanical properties of the B2 compound NiAl. *Int. Mater. Rev.* **38**, 193–232 (1993).
43. Jiao, Z. B. *et al.* Effects of Mn partitioning on nanoscale precipitation and mechanical properties of ferritic steels strengthened by NiAl nanoparticles. *Acta Mater.* **84**, 283–291 (2015).

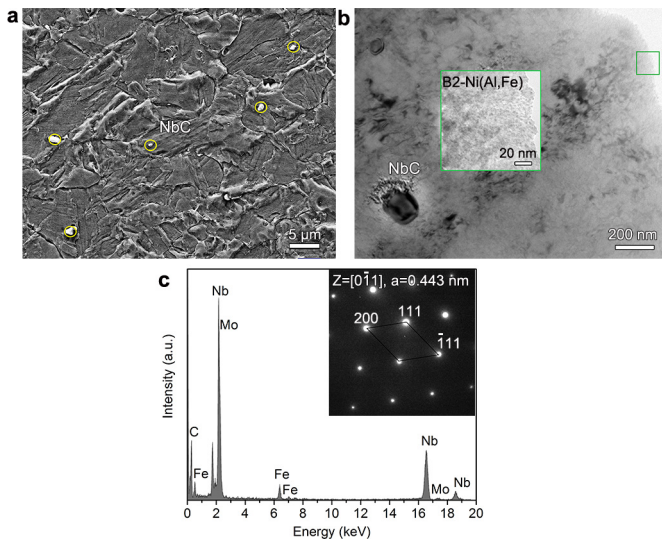


**Extended Data Figure 1 | Comparison of ultimate tensile stress and raw material cost between the typical ultra-high-strength steels and the Ni(Al,Fe)-maraging steels.** The typical ultra-high-strength steels include the commercially successful 18 wt% Ni maraging steels (Ni18Co9Mo5, wt%)<sup>1</sup>, Co-free maraging steels (Ni18.5Mo4Ti, wt%)<sup>2</sup>, W-strengthened steel (Ni19W4.2Ti1.2, wt%)<sup>29</sup>, and some commercial ultra-high-strength steels (for example, Ni11Co13Cr3, wt%)<sup>30</sup>.

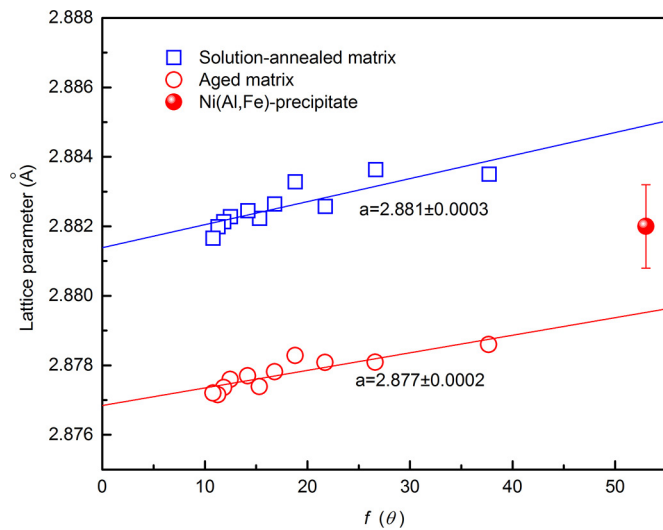


**Extended Data Figure 2 | The chemical compositions of the precipitates with different shapes and sites. a, b,** The selected precipitates (a) and corresponding chemical compositions (b). Precipitate A: round precipitates far away from Mo/C-decorated dislocations. Precipitate B: rod precipitates far away from Mo/C-decorated dislocations. Precipitate C: round/rod precipitates attached to Mo/C-decorated dislocations. The errors are standard deviations of the mean.





**Extended Data Figure 4 | NbC precipitated in the solution-annealed specimen.** **a**, Scanning electron microscope image of the solution-annealed steel showing the presence of coarse primary NbC (0.5–2  $\mu\text{m}$ ; yellow circles). **b**, TEM image of the aged steel showing co-existence of NbC and Ni(Al,Fe) precipitates. The inset highlights the Ni(Al,Fe) precipitates in a local region of **b**. **c**, Energy dispersive spectroscopy and SAED patterns (the inset in **c**) of the large precipitate in **b**, confirming that the precipitate is MC-type (that is, a face-centred cubic metal carbide with metal-to-carbon ratio 1) NbC. Owing to its small volume fraction and large size, NbC was not observed in the APT characterization.



**Extended Data Figure 5 | Lattice parameters of the matrix and the B2 versus  $f(\theta)$ .**  $f(\theta) = \cos^2(\theta) \times (1/\sin\theta + 1/\theta)/2$ , where  $\theta$  is the Bragg angle for each peak<sup>34</sup>. The best lattice parameter  $a$  was obtained at  $f(\theta) = 0$ . The errors of the lattice parameters are associated with the errors in experimental measurements of  $\theta$ .

**Extended Data Table 1 | Diffusion coefficients of Fe, Ni, Al and Mo in  $\alpha$ -Fe at 500 °C**

Element	Diffusion coefficient at 500 °C ( $\text{m}^2\text{s}^{-1}$ )	Diffusion length for 3h (nm)	Expression	Reference
Mo	$1.11 \times 10^{-21}$	6.9	$126e^{-282000/RT}$	35
Fe	$3.52 \times 10^{-21}$	12.3	$2.76e^{-250000/RT}$	36
Al	$2.63 \times 10^{-20}$	33.7	$5.35e^{-241000/RT}$	37
Ni	$3.89 \times 10^{-21}$	13.0	$1.40e^{-245000/RT}$	38

Data is taken from references 35–38.